

Single-epoch VLBI imaging study of bright active galactic nuclei at 2 and 8 GHz

A. B. Pushkarev^{1,2,3}, Y. Y. Kovalev^{4,1}

¹ Max-Planck-Institut für Radioastronomie, Auf dem Hügel 69, 53121 Bonn, Germany
e-mail: apushkar@mpi.fr.de

² Pulkovo Astronomical Observatory, Pulkovskoe Chaussee 65/1, 196140 St. Petersburg, Russia

³ Crimean Astrophysical Observatory, 98409 Nauchny, Ukraine

⁴ Astro Space Center of Lebedev Physical Institute, Profsoyuznaya 84/32, 117997 Moscow, Russia
e-mail: yyk@asc.rssi.ru

Received 4 April 2012; accepted 22 May 2012

Abstract

Aims. We investigate statistical and individual astrophysical properties of active galactic nuclei (AGN), such as parsec-scale flux density, core dominance, angular and linear sizes, maximum observed brightness temperatures of VLBI core components, spectral index distributions for core and jet components, and evolution of brightness temperature along the jets. Furthermore, we statistically compare core flux densities and brightness temperature as well as jet spectral indices of γ -ray bright and weak sources.

Methods. We used 19 very long baseline interferometry (VLBI) observing sessions carried out simultaneously at 2.3 and 8.6 GHz with the participation of 10 Very Long Baseline Array (VLBA) stations and up to 10 additional geodetic telescopes. The observations span the period 1998–2003.

Results. We present here single-epoch results from high-resolution radio observations of 370 AGN. VLBI images at 2.3 and 8.6 GHz as well as Gaussian models are presented and analyzed. At least one-fourth of the cores are completely unresolved on the longest baselines of the global VLBI observations. The VLBI core components are partially opaque with the median value of spectral index of $\alpha_{\text{core}} \sim 0.3$, while the jet features are usually optically thin $\alpha_{\text{jet}} \sim -0.7$. Spectral index typically decreases along the jet ridge line due to the spectral aging, with a median value of -0.05 mas^{-1} . Brightness temperatures are found to be affected by Doppler boosting and reaching up to $\sim 10^{13}$ K with a median of $\sim 2.5 \times 10^{11}$ K at both frequencies. The brightness temperature gradients along the jets typically follow a power law $T_b \propto r^{-2.2}$ at both frequencies. 147 sources (40%) positionally associated with γ -ray detections from the *Fermi* LAT Second Source Catalog are found to have higher core flux densities and brightness temperatures, and are also characterized by less steep radio spectrum of the optically thin jet emission.

Key words. galaxies: active – galaxies: jets – quasars: general – radio continuum: galaxies

1. Introduction

The long-term VLBI project RDV (Research & Development – VLBA) is aimed at observations of bright, flat-spectrum, compact extragalactic radio sources. The project started in 1997 under coordination of NASA and NRAO. The simultaneous observations at 2.3 and 8.6 GHz are carried out bi-monthly making up five to six sessions per year with participation of all ten 25 m VLBA antennas and up to ten geodetic stations (see for details Petrov et al. 2009). The participation of the southern antennas such as HartRAO (South Africa) and TIGO (Chile) allowed to improve the uv -coverage of low-declination sources. One of the initial goals of the project was focused on estimating precise absolute positions of compact sources and improving the International Celestial Reference Frame (ICRF; Ma et al. 1998), which was extended up to 776 sources (Fey et al. 2004) and later to 3414 radio astronomical objects making the ICRF2 (Boboltz et al. 2010). The second goal was addressed to precise geodesy and determination of antenna reference point changes associated with the motion of tectonic platforms (Petrov et al. 2009).

We have successfully used the same data for astrophysical studies of active galactic nuclei (AGN). We took the data from

the NRAO archive¹. Since the project was initially oriented on geodesy and astrometry, the primary information was in the measured phases of the registered signals, whereas for us both the phases and amplitudes are equally important for restoring and analyzing the images. We contacted staff of the non-VLBA stations and received valuable information of system equivalent flux densities (SEFD) and system temperatures at epochs of observations. Note, our imaging results promise to provide feedback for astrometry, i.e., for improving the accuracy of absolute position of the sources taking into account their milliarcsecond structure.

In each experiment, about 100 active galactic nuclei are scheduled. Currently, the total number of sources within RDV project is reaching 1000. The main selection criteria for the RDV targets were brightness and compactness of the sources (Petrov et al. 2009). In this paper, we present results of our imaging and analysis of raw archival RDV data for a sample of 370 objects (Fig. 1) coming from 19 sessions performed within the period 1998–2003. If a source was observed more than once we selected the epoch at which a dynamic range of the image was the highest. The sample is dominated by quasars, with the weak-lined BL Lacs and radio galaxies mak-

¹ <http://archive.nrao.edu>

ing up 8.3% and 7.8% of the sample, respectively. We used all 370 sources available from the reduced observations for the analysis, because as it was shown by Lister & Marscher (1997), the most effective approach of studying Doppler boosted sources such as AGN is based on investigation of samples with large number of objects. Otherwise, the selection effect may lead to incorrect conclusions about AGN properties as a class of radio sources. Chronologically, the RDV project was one of the first among other large VLBI imaging surveys covering altogether the frequency range from 2 to 86 GHz and including VLBA Calibrator Survey (VCS; Beasley et al. 2002; Fomalont et al. 2003; Petrov et al. 2005, 2006; Kovalev et al. 2007; Petrov et al. 2008), VLBI Space Observatory Program (VSOP; Fomalont et al. 2000; Dodson et al. 2008), VLBI Imaging and Polarimetry Survey (VIPS; Helmboldt et al. 2007; Petrov & Taylor 2011), Caltech-Jodrell Bank Flat-Spectrum sample (CJF; Pollack et al. 2003), complete sample of BL Lacertae objects (Gabuzda et al. 2000), VLBA 2 cm Survey (Kellermann et al. 1998) and Monitoring Of Jets in Active galactic nuclei with VLBA Experiments (MOJAVE; Lister et al. 2009a), VLBI Exploration of Radio Astrometry (VERA) and VLBA K-band (Petrov et al. 2007, 2012), International Celestial Reference Frame (ICRF; Lanyi et al. 2010; Charlot et al. 2010) and its extensions (Fey et al. 2004), and Coordinated Millimetre VLBI Array (CMVA; Lee et al. 2008) surveys.

First imaging results for early five 24-hour pre-RDV sessions with participation of only the VLBA antennas have been presented by Fey et al. (1996) and Fey & Charlot (1997, 2000). Imaging of some other RDV epochs prior to 1998 was also done by Piner et al. (2007). In this paper, we present and analyze our images from 19 experiments. VLBI maps for the majority of RDV experiments including maps presented in this paper are made available online²³⁴. Astrometric suitability for 80% of the ICRF sources was investigated by Charlot et al. (2008). The RDV observations proved to be successful for spectral index studies including opacity effect detections reported by Kovalev et al. (2008) and confirmed later by Sokolovsky et al. (2011). Another application, is measuring multi-epoch 8.6 GHz apparent speeds of the jet components. The initial kinematics results for 54 sources based on 8.6 GHz VLBI images in Radio Reference Frame Image Database from first five years (1994–1998) of data were obtained by Piner et al. (2007). Extending the period of observations up to ten years and enlarging a number of epochs up to 50 will both increase the accuracy of apparent speed measurements and allow to investigate possible jet acceleration (Piner et al. 2012).

Observational material of RDV project has a number of advantages in comparison with the data from many large VLBA experiments cited above: (i) improved coverage of uv -plane; (ii) simultaneous dual-frequency mode; (iii) high time sampling (nearly every two months) for a subsample of about 60 sources. The last feature allows studying jet kinematics (Piner et al. 2007), while other two are important for the purposes of this paper, in which we discuss compactness of the sources, their spectral indices, brightness temperatures, and also compare these properties for γ -ray bright and weak sources.

Out of the 370 RDV sources presented in this paper, 147 objects have been positionally cross-identified with the high-confidence ($>4\sigma$) γ -ray detections associated with known AGN, according to the *Fermi* Large Area Telescope Second Source

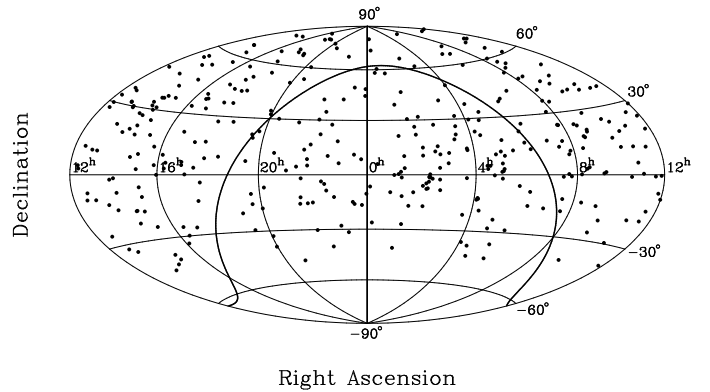


Figure 1. Sky distribution of 370 observed sources in Aitoff equal-area projection of the celestial sphere in equatorial coordinates. The thick line is the Galactic equator.

Catalog (2FGL; Abdo et al. 2011). These objects are both targets of follow-up observational VLBI sessions and prospects for establishing connections between γ -ray emission and parsec-scale jets observed in radio domain.

The structure of this paper is as follows: in § 2 we describe the observations and data reduction technique, including calibrating, imaging, and model-fitting procedures; in § 3 we discuss the results; and the main conclusions are summarized in § 4. Throughout the paper, the Λ CDM cosmological model with $H_0 = 70 \text{ km s}^{-1} \text{ Mpc}^{-1}$, $\Omega_m = 0.3$, and $\Omega_\Lambda = 0.7$ is adopted. Spectral index α is defined in the convention $S \propto \nu^\alpha$. All position angles are given in degrees east of north. We use the term “core” as the apparent origin of AGN jets that commonly appears as the brightest feature in VLBI images of blazars (e.g., Lobanov 1998; Marscher 2008).

2. Source sample, observational data and data processing

2.1. Source sample and its completeness

The sample of 370 sources includes 251 quasars (67.8%), 46 BL Lacertae objects (12.4%), 31 radio galaxies (8.4%), and 42 optically unidentified sources (11.4%). The redshifts are currently known for 306 objects (83%). The redshift distribution (Fig. 2) ranges from $z_{\min} = 0.00436$ for the galaxy J1230+1223 (M87) to $z_{\max} = 4.715$ for the quasar J1430+4204 with a median value of the distribution close to $z = 1$. The general characteristics of the sources such as object name, its alternative name, coordinates of J2000.0 right ascension and declination, optical class, redshift, and linear scale in parsecs per mas are listed in Table 1.

To investigate the completeness of the studied sample, we constructed a cumulative $\log N - \log S$ dependence (Fig. 3) for the studied RDV subsample in comparison with the Radio Fundamental Catalog⁵ (RFC) in the matched sky area, with declinations above -45° . The RFC provides (i) precise positions with milli-arcsecond accuracies, (ii) estimates of correlated flux densities at baselines from 1000 to 8000 km, and (iii) maps for thousands of compact radio sources produced by analysis of all available VLBI observations under absolute astrometry and geodesy programs. The RFC sample constructed from a blind survey is statistically flux density complete down to 200 mJy (Kovalev et al. 2007; Petrov et al. 2008). Note that the difference in 1–2 sources seen for the brightest objects is due to flux density

² <http://astrogeo.org/images>

³ <http://rorf.usno.navy.mil/rrfid.shtml>

⁴ <http://www.obs.u-bordeaux1.fr/BVID>

⁵ <http://astrogeo.org/rfc>

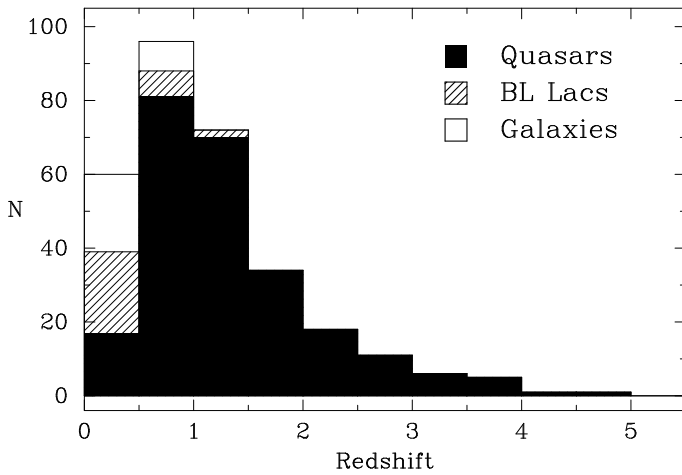


Figure 2. Redshift distribution of 306 sources with the median and maximum values 0.98 and 4.715, respectively.

variability and the fact that the RFC provides the flux densities averaged over all available epochs, while the RDV statistics is based on single-epoch measurements. As seen from Fig. 3, the studied RDV subsample is complete down to ~ 1.5 Jy. At lower flux densities, the sample is not statistically complete but representative of compact AGN due to the original selection strategy of the RDV project (Petrov et al. 2009).

2.2. Observational data

We have reduced and present here single-epoch imaging results of 19 observational 24-hour sessions (RDV11, 13, 15, 18, 21, 24, 27, 29, 30, 31, 32, 33, 34, 35, 36, 37, 38, 39, 41) carried out in a period since October 1998 through September 2003 using a global VLBI array of 18 to 20 stations including 10 VLBA antennas and 14 geodetic and EVN radio telescopes (Table 2) capable of recording the VLBA modes, with 8 to 10 non-VLBA stations in each session. The dates of observations are listed in first column in Table 4. The positions for all antennas given in geocentric coordinates are listed in Petrov et al. (2009), Table 3. The observations were performed in a standard dual-frequency geodetic mode, registering the signal in right circular polarization simultaneously at 2.3 GHz (S-band) and 8.6 GHz (X-band), and using 1-bit sampling. Each band was separated into four 8 MHz (4 MHz for RDV11) intermediate frequencies (IFs) giving a total observing bandwidth of 32 MHz (16 MHz for RDV11) at each band. The IFs spanned 140 MHz at S-band and 490 MHz at X-band (Table 3). The data were correlated with the VLBA correlator at the Array Operation Center in Socorro with 4 s accumulation periods. Most sources were observed during six scans of six minutes each, making a total tracking time of about 40 min. A few sources were observed up to 15 scans, making a total on-source time of about 60 min. The scans are scheduled over a number of different hour angles to maximize the (u, v) plane coverage. The median number of independent measurements of visibility function on individual interferometer baselines averaged within a scan is about 200. No special calibrators have been scheduled since all the target sources were compact and bright. More than 92% of the sources in 19 processed sessions have VLBI flux greater than 200 mJy (see Fig. 9, top panels).

Observations were scheduled using the automatic mode of SKED with some subsequent improvements to maximize mu-

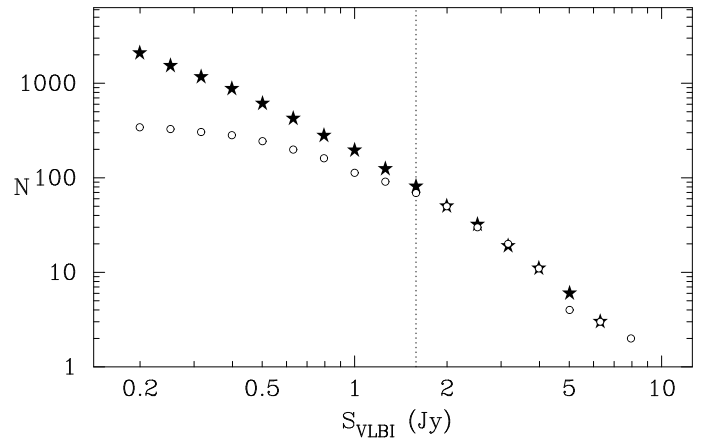


Figure 3. Cumulative $\log N - \log S$ dependence at 8.6 GHz for the studied RDV sample of 370 sources (open circles) in comparison with the Radio Fundamental Catalog (stars). The dotted line indicates a completeness level of about 1.5 Jy for the studied sample.

tual visibility, ensure adequate sky coverage, minimize slewing time, etc. The detailed description of the scheduling of the global geodetic VLBI sessions is discussed by Petrov et al. (2009).

The special feature of these observations is the use of sub-arrays. The involvement of the large number of stations located on different continents results in the fact that the antennas cannot simultaneously track the same target source altogether. To maximize the on-source time at each station during the whole experiment, the array of radio telescopes is divided into several subarrays such that to ensure that a source is visible for every station in a corresponding subarray during a particular scan. The number of subarrays ranges from 6 to 8 in the reduced experiments. Note that each antenna is included not only in some particular subarray, but in several ones for different scans. Thus, the majority of sources are observed with almost all antennas participating in a session. The exceptions are the high-declination sources for the southern stations and vice versa.

The 5 m VLBI antenna MV-3 GGAO near Washington also took part in the observations but we did not use the data from this site because of its extremely high noise level ($\text{SEFD} \gtrsim 5 \times 10^4$ Jy). In addition, GGAO in a number of experiments was tagged along after the schedule was generated using other stations in a session. GGAO was added to each scan that the antenna could slew to in time, and the scan length for GGAO was set to the maximum of all the stations already participating in the scan. This resulted in a significant number of non-detections on the GGAO baselines.

The Southern hemisphere antennas, 26 m radio telescope HartRAO in South Africa (latitude of -26°) and 6 m TIGO antenna in Concepcion, Chile (latitude of -36°), have participated in 15 out of the 19 analyzed observational sessions. This significantly increased the resolution in the North-South direction and allowed us to image low-declination sources with almost circular restoring beam. The contribution of data from even such a small antenna as TIGO can significantly improve the quality of the final image (Fig. 4) if the source is bright ($S > 0.5$ Jy).

On average, increasing the number of antennas in the array from 10 (VLBA) to 18–20 (global VLBI) allowed to:

- increase the number of possible baselines by a factor of ~ 2.5 ,
- increase the angular resolution by a factor of ~ 1.5 ,

Table 1. Parameters of observed sources.

Source	IVS name	Right Ascension J2000.0	Declination J2000.0	Optical class	z	Scale pc mas ⁻¹	2FGL member
(1)	(2)	(3)	(4)	(5)	(6)	(7)	(8)
J0006–0623	0003–066	00 06 13.892887	–06 23 35.33545	B	0.347	4.913	...
J0011–2612	0008–264	00 11 01.246737	–26 12 33.37719	Q	1.093	8.163	...
J0017+8135	0014+813	00 17 08.474901	+81 35 08.13655	Q	3.387	7.407	...
J0019+7327	0016+731	00 19 45.786379	+73 27 30.01753	Q	1.781	8.450	...
J0022+0608	0019+058	00 22 32.441214	+06 08 04.26889	B	Y
J0027+5958	0024+597	00 27 03.286191	+59 58 52.95918	U
J0035+6130	0032+612	00 35 25.310644	+61 30 30.76129	U
J0050–0929	0048–097	00 50 41.317382	–09 29 05.21043	B	Y
J0059+0006	0056–001	00 59 05.514929	+00 06 51.62077	Q	0.717	7.215	...
J0102+5824	0059+581	01 02 45.762379	+58 24 11.13659	Q	0.644 ^a	6.902	Y

Columns are as follows: (1) J2000.0 IAU name; (2) IVS name (B1950.0 IAU name or alias); (3) right ascension (J2000.0) in hours, minutes and seconds; (4) declination (J2000.0) in degrees, minutes and seconds; (5) optical classification according to Véron-Cetty & Véron (2006), where Q is quasar, B is BL Lacertae object, G is active galaxy, U is unidentified, (6) redshift as given by Véron-Cetty & Véron (2006), the a flag indicates the redshift is from Sowards-Emmerd et al. (2005), b – from Carilli et al. (1998), c – from Drake et al. (2004), d – from Afanasiev et al. (2003), e – from von Montigny et al. (1995), f – from Nilsson et al. (2008), g – from Best et al. (2003), h from Hewitt & Burbidge (1989), k from Snellen et al. (2002b) l from Snellen et al. (2002a); (7) angular scaling conversion in parsecs per milliarcsecond; (8) membership in the *Fermi* LAT Second Source Catalog according to Abdo et al. (2011). The coordinate positions are taken from the Radio Fundamental Catalog (<http://astrogeo.org/rfc>) as derived from analysis of all VLBI observations made in absolute astrometry and geodesy mode (Beasley et al. 2002; Fomalont et al. 2003; Petrov et al. 2005, 2006; Kovalev et al. 2007; Petrov et al. 2008). Table 1 is published in its entirety in the electronic version of the *Astronomy & Astrophysics*. A portion is shown here for guidance regarding its form and content.

Table 2. Antennas participating in RDV observations.

Station	Location	Code	Diameter m
Algonquin Park	Canada	AP	46
Brewster	USA	BR	25
Fort Davis	USA	FD	25
Gilcreek	USA	GC	26
Green Bank	USA	GN	20
Hancock	USA	HN	25
HartRAO	South Africa	HH	26
Kitt Peak	USA	KP	25
Kokkee	USA	KK	20
Los Alamos	USA	LA	25
Matera	Italy	MA	20
Mauna Kea	USA	MK	25
Medicina	Italy	MC	32
North Liberty	USA	NL	25
Noto	Italy	NT	32
Ny Alesund	Norway	NY	20
Onsala	Sweden	ON	20
Owens Valley	USA	OV	25
Pie Town	USA	PT	25
St. Croix	USA	SC	25
Concepcion	Chile	TC	6
Tsukuba	Japan	TS	32
Westford	USA	WF	18
Wetzell	Germany	WZ	20

– decrease the noise level of the resultant VLBI image by a factor of ~ 2 .

The maximum projected baseline of about 12300 km between Owens Valley (VLBA) and HartRAO realized in RDV experiments is close to the limit of Earth-based VLBI observations. In Fig. 5, we show the comparison of the typical (u, v) coverage at 8.6 GHz provided by the VLBA and the whole array used for high-, medium-, and low-declination sources. The correspond-

Table 3. The range of used frequencies.

IF	Frequency range ^a , [MHz]
1	2232.99 – 2240.99
2	2262.99 – 2270.99
3	2352.99 – 2360.99
4	2372.99 – 2380.99
5	8405.99 – 8413.99
6	8475.99 – 8483.99
7	8790.99 – 8798.99
8	8895.99 – 8903.99

^a S-band IFs have been shifted up 12 MHz since RDV27 session (2001.04.09) to get further away from direct broadcast satellite band.

ing spatial frequency plane coverages at 2.3 GHz are virtually identical but scaled accordingly.

2.3. Data processing

Initial calibration was performed with the NRAO Astronomical Image Processing System (AIPS; Greisen 2003) applying techniques adopted for subarrayed data sets. The individual IFs were processed separately throughout the data reduction, and were averaged together when making the final images. The antenna gains and system temperatures measured during the sessions were used for the amplitude calibration. For some of the non-VLBA stations, there was no direct information about the antenna’s gain at the epoch of an experiment. In such cases we estimated the DPFU parameter (gain) for each band using the information provided by the staff of observatories about the SEFD measured on a date closest to the epoch of observations (within several days) and the system temperature averaged over the current session. Global gain correction factors for each station for each IF have been derived from statistical results of self-calibration for all the sources within an experiment taking into account the well measured VLBA antenna gains. If the me-

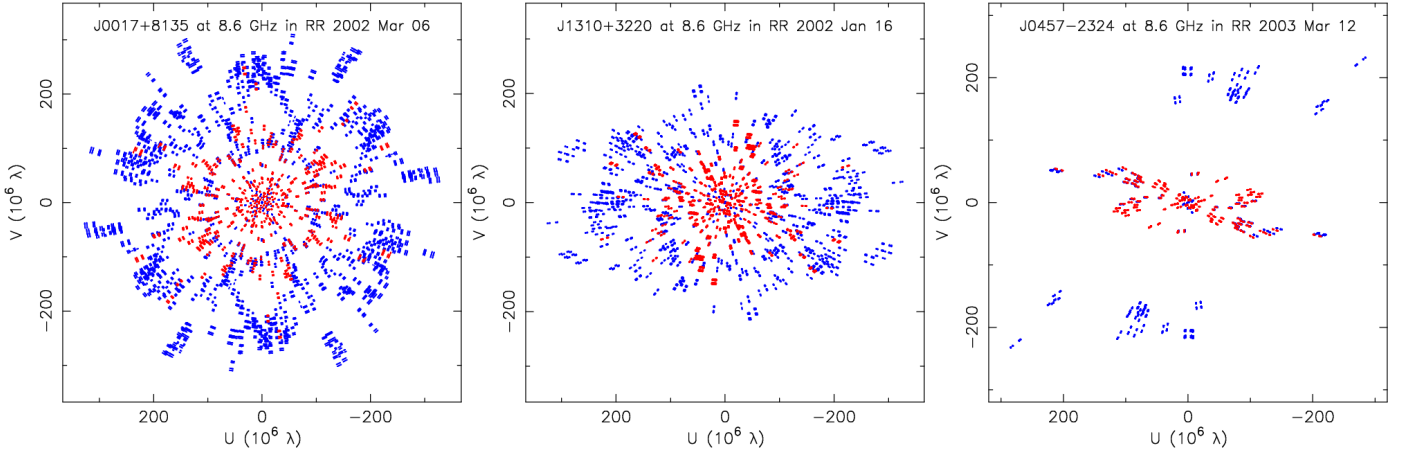


Figure 5. Coverages of the (u, v) plane at 8.6 GHz for a high-declination (J0017+8135, *left*), medium-declination (J1310+3220, *middle*), and low-declination (J0457–2324, *right*) source with the baseline projections produced by the VLBA antennas only (red dots) and the global VLBI array (red + blue dots).

Table 4. Observing log with non-VLBA telescope gains. VLBA antennas participated in all the sessions.

Date	2.3/8.6 GHz DPFU ^a , [mK Jy ⁻¹]													
	AP	GC	GN	HH	KK	MA	MC	NY	NT	ON	TC	TS	WF	WZ
1998/10/01		85/125	78/70		70/41		140/128	24/69		23/45			43/39	
1999/03/08		95/67	49/76	33/21	60/47		138/152	30/77		24/48			47/40	63/68
1999/05/10		119/74		36/38	60/43		131/143	31/72		23/34			43/36	66/79
1999/12/20		69/84	50/72	38/30	60/47		140/146	30/77		23/45		176/269	45/38	57/38
2000/05/22		88/74		36/24	67/39	27/45	128/118	34/73				223/271	46/37	71/80
2000/12/04		82/94		36/22	65/36	47/49	180/134	32/76				205/269	44/39	68/82
2001/04/09		95/80		43/26	63/35	68/51	120/132	32/69				214/242	47/38	68/81
2001/07/05		96/69		34/20	39/38		126/124	31/67				207/207	54/34	62/72
2001/10/29				36/15	39/41	54/40	119/114					154/163	60/35	65/72
2002/01/16		98/74			42/41		139/101	46/61		39/32		211/236	46/33	61/53
2002/03/06		87/81			41/44		132/116		-127	36/36		204/203	45/34	61/71
2002/05/08	300/188	91/76		37/16	67/42	66/42	134/113						43/34	66/78
2002/07/24		63/67			71/42	51/44	-118	61/66		28/35	5/8		53/34	62/69
2002/09/25		98/71			72/42	60/52	129/83			24/42	5/8	309/122	56/34	71/70
2002/12/11		98/66			59/40	32/41	148/133	62/67		31/30	4/6		53/34	65/69
2003/03/12					53/38	20/45	140/114			28/34	5/8	227/335	77/33	62/72
2003/05/07					53/44	29/45	129/126			30/30	4/8	261/212	61/36	64/81
2003/06/18					57/42	-47				31/39	6/9	220/183	66/31	-78
2003/09/17		86/74			61/46			26/54		20/36		175/171	27/37	75/95

^a Efficiency (degrees per flux unit) of a radio telescope in right circular polarization in zenith direction. In all cases the gain curve is assumed to be flat.

dian value of the gain correction distribution deviated more than 10% from 1, the whole calibration procedure was performed over again applying the corresponding corrections by running the AIPS task CLCOR prior to the stage of phase calibration. We estimate the accuracy of amplitude calibration to be at the level of $\sim 10\%$. The non-VLBA station sensitivities obtained from the log-files and then defined more accurately from the gain correction technique are listed in Table 4.

Because the phase calibration tones were not available for all the stations (non-VLBA stations do not have phase-cal detectors), the phase corrections for station-based residual delays and delay rates were found and applied using the AIPS task FRING in two steps. First, the manual fringe fitting was run on a short interval of 1 or 2 minutes on a bright compact source to determine the relative instrumental phase and residual group delay for each individual IF. To find the solution for all antennas being split-

ted into subarrays, it required running the procedure on several different scans. Secondly, the global fringe fitting was run specifying 4 min solution interval, a point-like source model, and a signal-to-noise cutoff of 5 to omit noisy solutions. The amount of bad solutions was typically at a level of (8–10)% at X-band and (10–13)% at S-band.

Amplitude bandpass calibration has not been applied because it had no significant effect on the dynamic range of final images. We used the AIPS task SPLIT to write the fully calibrated data for each individual source to separate X- and S-band FITS-files averaging data in frequency within each of four IFs at each band, and making no averaging in time. First, phase self-calibration with a point-source model was done using the AIPS task CALIB which provides: (i) a possibility to find the first solution using all IFs, (ii) automatic flagging the data with low signal-to-noise ratio.

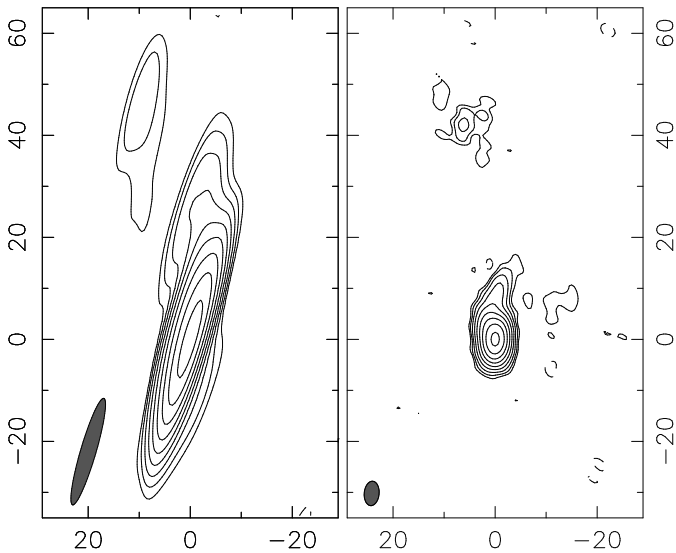


Figure 4. Naturally weighted CLEAN images at 2.3 GHz of the low-declination source J0403-3605 without (*left*) and with the data (*right*) from TIGO antenna. The contours are shown at the same levels, starting from 2 mJy beam^{-1} and increasing by a power of 2. The axes of each image are given in milliarcseconds. The shaded ellipse in the lower left corner of each image indicates the FWHM of the restoring beam.

CLEANing (Högbom 1974), phase and amplitude self-calibration (Jennison 1958; Twiss et al. 1960), and hybrid imaging (Readhead et al. 1980; Schwab 1980; Cornwell & Wilkinson 1981) were performed in the Caltech DIFMAP (Shepherd 1997) package using an automated approach suggested by G. Taylor (Pearson et al. 1994), which we adapted for the RDV data set. In all cases, a point-source model was used as an initial model for the iterative procedure. Final maps were produced applying natural weighting of the visibility function. The spanned bandwidth of the four IFs in each band is relatively small (6% of fractional bandwidth in both bands), therefore no spectral correction technique has been applied. In the model fitting, also done in DIFMAP, we used a minimum number of circular (and in some cases elliptical) Gaussian components that being convolved with the restoring beam, adequately reproduce the constructed brightness distribution.

3. Results

3.1. Calibrated VLBI images

Final, naturally weighted VLBI images at 2.3 and 8.6 GHz for 370 sources are shown in Fig. 6. The dynamic range of the images determined as a ratio of the peak flux density to the rms noise level ranges from 66 to 7042 with a median of ~ 1200 at X-band, and ranges from 106 to 4789 with a median of ~ 1000 at S-band. The typical rms noise level is $\sim 0.4 \text{ mJy beam}^{-1}$ at X-band and $\sim 0.5 \text{ mJy beam}^{-1}$ at S-band.

In Table 5, we summarize the VLBI map parameters: (1) source name in J2000.0 notation; for X-band: (2) peak flux density in Jy beam^{-1} ; (3) lowest contour level in mJy beam^{-1} ; (4) flux density integrated over entire map in Jy; (5) flux density of the most compact fraction in Jy as measured from the longest baselines; (6) major axis of FWHM of restoring beam in milliarcsec; (7) minor axis of FWHM of restoring beam in milliarcsec; (8) position angle of major axis of restoring beam in

degrees; columns (9)–(15) are the same as (2)–(8) but for S-band. Flux densities shown in columns (4) and (11) were calculated as a sum of all CLEAN components over VLBI image. Columns (5) and (12) give the flux densities of the unresolved fractions S_{unres} and are estimated as the median of the visibility function amplitudes measured at spatial (u, v) radius $r_{uv} = (u^2 + v^2)^{1/2} > 270 \text{ M}\lambda$ for X-band and $r_{uv} > 72 \text{ M}\lambda$ for S-band, corresponding to the range between 0.8 and 1.0 of the maximum projected spacing. For 15 sources at X-band and 6 sources at S-band, no estimates of unresolved flux density are given because no data were available on the baselines used for the calculations.

In addition to Table 5, all calibrated data including FITS files of naturally weighted CLEAN images, FITS files with (u, v) data sets, images in postscript and GIF-formats, plots of correlated flux density versus baseline length projection, and values of total VLBI flux density for all the sources at all available epochs listed in Table 4 are accessible online through HTML interface.⁶

3.2. Parsec-scale structure modeling

The observed sources have very complex three-dimensional structure at parsec and deparsec scales. But being located at cosmological distances they provide us with a possibility to investigate only their two-dimensional brightness distribution in the plane of the sky, which can be modeled by a limited number of Gaussian components. The number of components is usually determined by reconciling two opposite conditions: (i) it should be minimal; (ii) all the components being convolved with the restoring beam, adequately reproduce the general structure of the obtained brightness distribution. Typical morphology of the sources is represented by one-sided core-jet structure implying strong selection effects and Doppler boosting of jet emission (Cohen et al. 2007). Only 11 sources (3% of the sample) have two-sided structure detected in the S/X images. There are also extreme cases when (i) a source is highly compact without any indications of a jet, presumably because of lack of spatial resolution and/or sensitivity of the interferometer at the observed frequency; (ii) a source has a prominent jet that is resolved even in a transverse direction. In Fig. 7, we plot the images of J1935+2031 and J0738+1742 as examples.

Structure modeling of all sources was performed with the procedure *modelfit* in Difmap package by fitting several circular Gaussian components to the self-calibrated visibility data and minimizing χ^2 in the spatial frequency plane. Elliptical Gaussian components were only applied in those cases when the use of circular Gaussian component resulted in the appearance of axisymmetric noise on the residual map near the modeled component. The model fits listed in Table 6 provide flux densities, positions, and sizes for the bright and distinct jet features. All the positions are given with respect to the core component. The quality of model fitting is generally quite good as it seen in Fig. 8, where we plot the total flux density of the Gaussian components of the fit and CLEANed flux density calculated as a sum of all CLEAN components from the image.

3.3. Compactness

One of the main goals of the RDV program was to construct the Radio Reference Frame. The sources included in the observing program thus have to lie at cosmological distances, be bright and compact, i.e., to radiate the emission from the extremely limited

⁶ See <http://vlbi.crao.crimea.ua/SX>

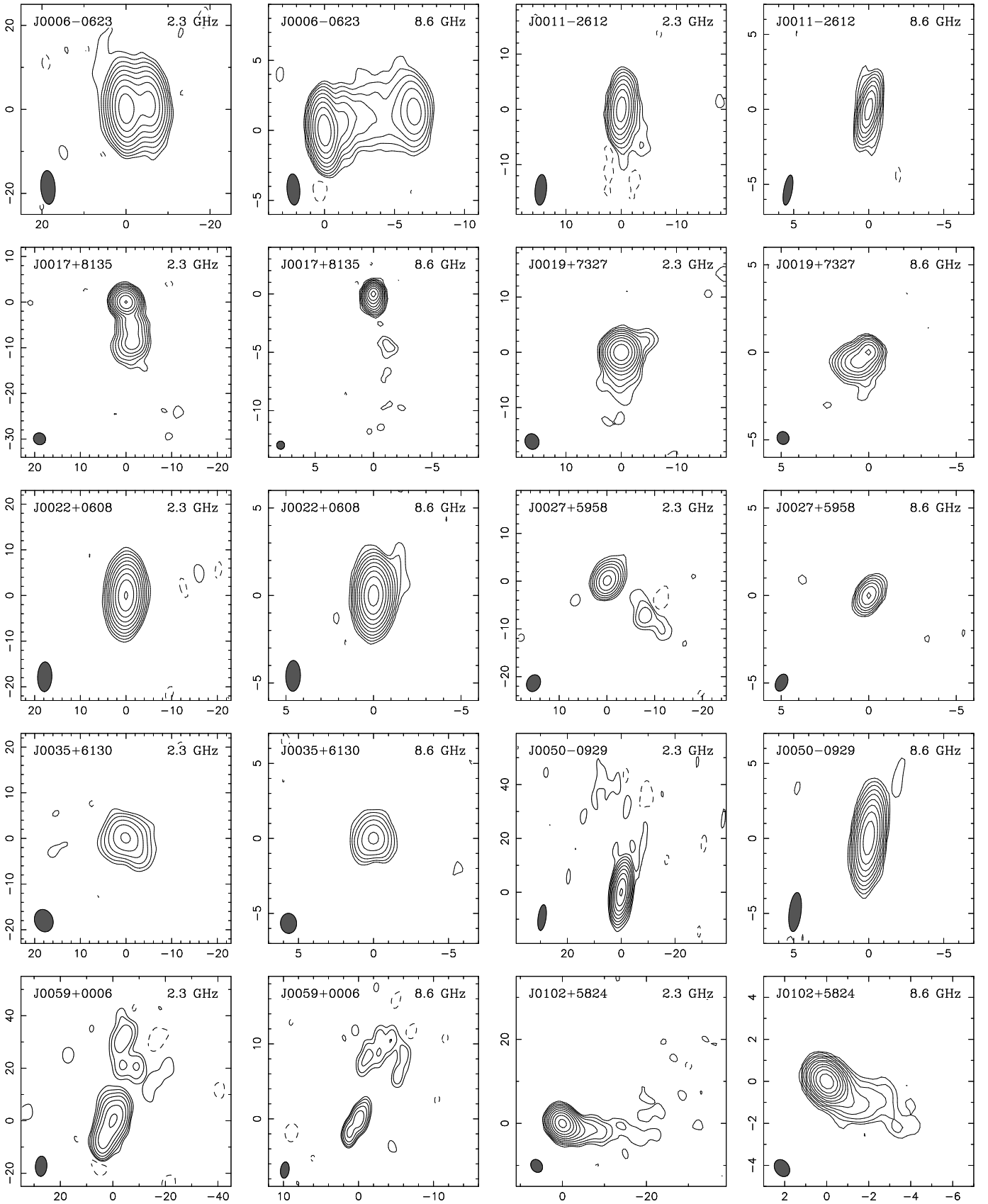


Figure 6. One-epoch 2.3 and 8.6 GHz VLBI images of 370 active galactic nuclei. Image parameters are listed in Table 5. Gaussian models fitted to the visibility data at each frequency are listed in Table 6. The scale of each image is in milliarcsecond. The shaded ellipse in the lower left corner indicates the FWHM of the restoring beam (with natural weighting). The contours are plotted at increasing factors of 2 times the lowest contour drawn at 3σ level. A single negative contour equal to the bottom positive contour is also shown. A cell size of 0.2 and 0.5 mas per pixel was used for 8.6 and 2.3 GHz maps, respectively. Fig. 6 is available in its entirety in the electronic version of the *Astronomy & Astrophysics*.

Table 5. Parameters of VLBI maps.

Source (1)	2.3 GHz							8.6 GHz						
	peak Jy bm^{-1} (2)	clev mJy bm^{-1} (3)	S_{VLBI} Jy (4)	S_{unres} Jy (5)	B_{min} mas (6)	B_{maj} mas (7)	B_{PA} deg (8)	peak Jy bm^{-1} (9)	clev mJy bm^{-1} (10)	S_{VLBI} Jy (11)	S_{unres} Jy (12)	B_{min} mas (13)	B_{maj} mas (14)	B_{PA} deg (15)
J0006–0623	1.33	3.12	2.33	0.66	3.42	8.03	4	1.41	2.92	2.07	1.18	0.91	2.23	4
J0011–2612	0.39	1.90	0.41	0.36	2.06	5.56	–5	0.31	1.60	0.34	0.27	0.56	2.03	–10
J0017+8135	0.52	0.96	0.76	0.40	2.55	2.71	54	0.49	0.76	0.75	0.29	0.68	0.69	7
J0019+7327	0.57	1.20	0.76	0.35	2.51	2.86	20	0.15	1.00	0.34	0.13	0.68	0.74	19
J0022+0608	0.42	0.79	0.45	0.40	3.12	6.50	–2	0.41	0.58	0.44	0.35	0.84	1.76	–1
J0027+5958	0.07	0.90	0.08	0.07	2.81	3.63	–23	0.06	0.90	0.07	...	0.65	1.02	–24
J0035+6130	0.07	2.06	0.11	0.09	4.01	5.00	19	0.08	1.94	0.11	0.07	1.07	1.34	2
J0050–0929	0.53	1.93	0.58	0.45	2.97	9.62	–8	0.70	1.65	0.75	0.61	0.80	2.62	–7
J0059+0006	0.42	5.80	1.17	0.25	4.38	7.68	–4	0.16	5.40	0.43	0.06	1.14	2.18	–8
J0102+5824	0.61	0.92	0.81	0.42	2.63	3.25	32	1.55	0.88	1.68	1.46	0.67	0.87	35

Columns are as follows: (1) source name (J2000.0), (2) peak flux density in image, (3) lowest contour in image, (4) total flux density from VLBI map, (5) flux density from the most compact component on map, (6) FWHM minor axis of restoring beam, (7) FWHM major axis of restoring beam, (8) position angle of major axis of restoring beam, (9)–(15) the same as (2)–(8), respectively. Table 5 is published in its entirety in the electronic version of the *Astronomy & Astrophysics*. A portion is shown here for guidance regarding its form and content.

Table 6. Source models.

Source (1)	B (2)	S mJy (3)	r mas (4)	φ deg (5)	Maj. mas (6)	Ratio (7)	P.A. deg (8)
J0006–0623	S	1527	1.87	0.93	–37
		46	2.96	–55	...	1.00	...
		772	5.56	–77	2.79	1.00	...
	X	1551	0.81	0.34	7
		112	1.26	–68	0.50	1.00	...
		115	2.23	–65	1.58	1.00	...
128		5.34	–76	2.77	1.00	...	
J0011–2612	S	401	0.57	1.00	...
		327	0.26	1.00	...
	X	327	0.26	1.00	...

Columns are as follows: (1) source name (J2000.0), (2) frequency band, (3) fitted Gaussian flux density, (4) position offset from the core component, (5) position angle of the component with respect to the core component, (6) FWHM major axis of the fitted Gaussian, (7) axial ratio of the fitted Gaussian, (8) major axis position angle of the fitted Gaussian. Table 6 is published in its entirety in the electronic version of the *Astronomy & Astrophysics*. A portion is shown here for guidance regarding its form and content.

sky area. The best candidates for such objects are active galactic nuclei, which easily satisfy the aforementioned criteria. The compactness of blazars at arcsecond scale derived as $S_{\text{VLBI}}/S_{\text{tot}}$, where S_{tot} is the single-dish flux densities and S_{VLBI} is the integrated flux density from a VLBI image, is at a very high level of ~ 0.9 at 2 and 8 GHz as initially reported by Popov & Kovalev (1999) for small sample of 20 sources and later confirmed by Kovalev et al. (2005) for a complete sample of 250 flat-spectrum AGN observed with the VLBA at 15 GHz. This implies that nearly all of the emission from these sources is generated on milliarcsecond scale, probed by VLBI observations, and contribution from extended emission (kiloparsec scale) is typically negligible.

The compactness of the sources from our sample at milliarcsecond scale, determined as a ratio of S_{unres} to S_{VLBI} , distributions of which are presented in Fig. 9, is statistically lower

(Fig. 10, top panels) with median values of 0.51 at 2.3 and 8.6 GHz (Table 8). According to both K-S and T-test, the distributions are indistinguishable. At higher frequencies, the VLBI compactness is also at the similar level. Thus, 68% of the sample of 250 extragalactic radio sources observed at 15 GHz have the compactness greater than 0.5 (Kovalev et al. 2005). The median value of compactness at 86 GHz is about 0.5 as reported by Lee et al. (2008).

Note that overwhelming majority of the sources are also strong core dominated (Fig. 10, bottom panels). In 50% of sources, the emission from the core region accounts for more than 75% of the total VLBI flux. The information on S_{VLBI} , S_{unres} , and compactness will be useful for selecting the best candidates (highly-compact bright sources) to be studied with the *RadioAstron* space VLBI mission (Kardashev 1997). At the same time, there is a fraction of the sources with the opposite properties, i.e., strong jets (M87, 3C 120, etc.), which are of particular interest for detailed astrophysical studies of their extended outflows at parsec scales.

3.4. VLBI core properties

We define VLBI core as a compact, bright emitting region at the narrow end of the jet, where it becomes optically thick. Typically, VLBI cores are often unresolved along one or both axes of the restoring beam and have a flat radio spectrum. Being usually the brightest feature of the source it is placed by the phase self-calibration procedure to the center of the map. In fact, in such a case, the core component has always very small but nonzero shift from the phase center because of the close presence of other bright components down the jet. Significant offsets of the VLBI core components with respect to the phase center of an image are rare and happen when one of the jet components is brighter than the core. This kind of structure has been found for 18 sources at X-band, and for 27 ones at S-band.

Model fitting enabled to measure flux densities and sizes of the core components. The distributions of the core flux densities are plotted in Fig. 11 (top panels). Due to the high compactness of the cores they are often unresolved. We consider the core to be unresolved if the size of a circular Gaussian component or at least one of the axes of an elliptical Gaussian component

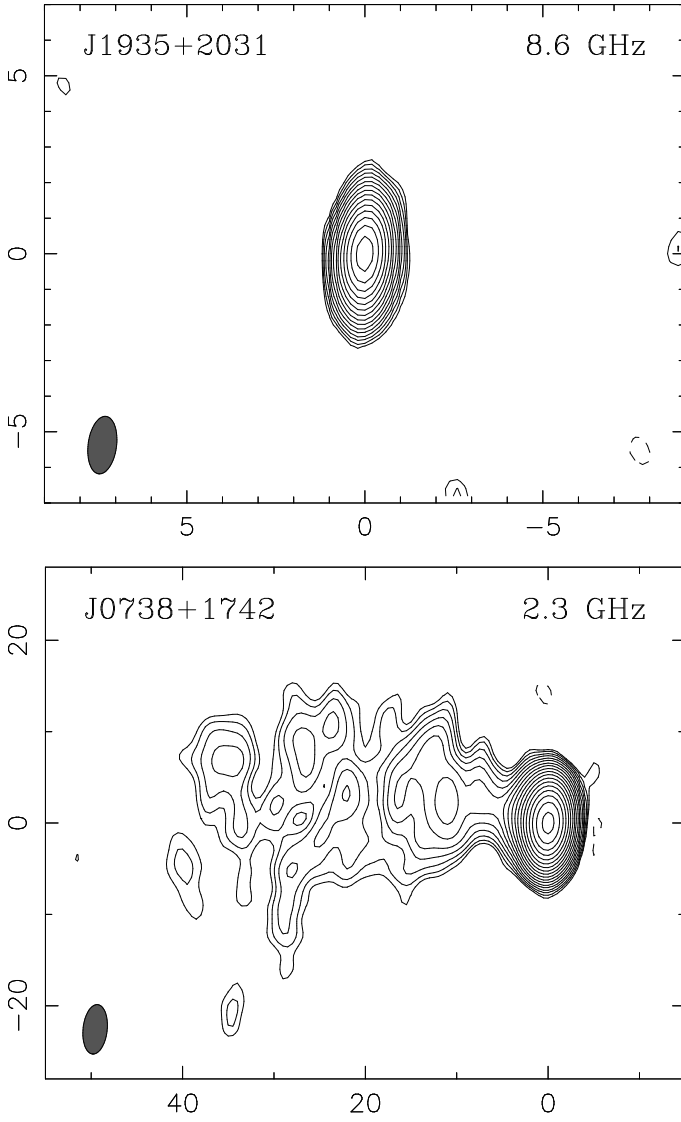


Figure 7. Naturally weighted CLEAN images of J1935+2031 at 8.6 GHz (*top*, dynamic range of 570) and J0738+1742 at 2.3 GHz (*bottom*, dynamic range of 1750) as examples of highly compact and jet-resolved sources, respectively. The axes of each image are given in milliarcseconds. The shaded ellipse in the lower left corner indicates the FWHM of the restoring beam.

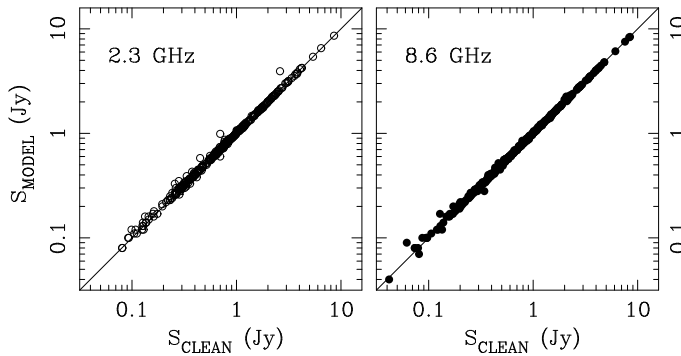


Figure 8. Total flux density from Gaussian fits versus total flux density from VLBI CLEAN image for the data at 2.3 GHz (*left*) and 8.6 GHz (*right*).

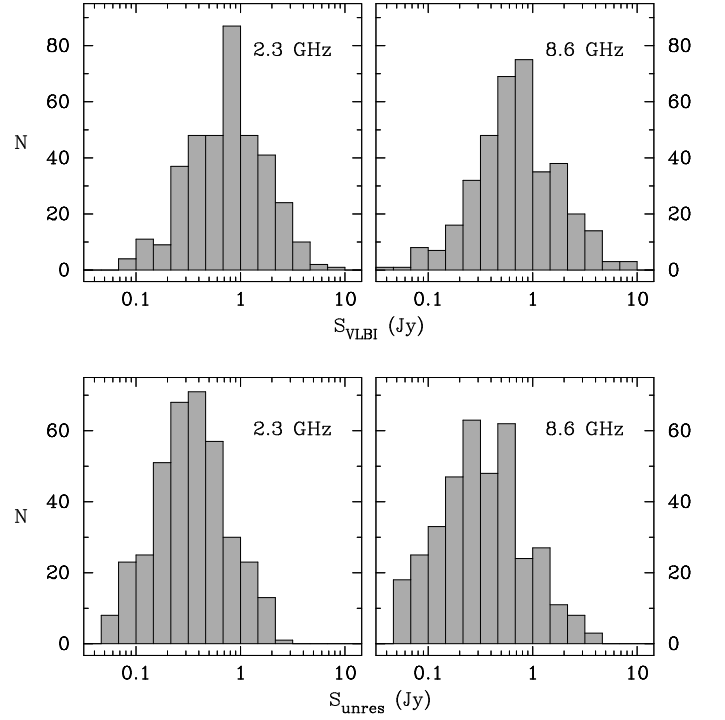


Figure 9. Distributions of the VLBI flux density S_{VLBI} (*top panels*), and the flux density of the most compact component, S_{unres} (*bottom panels*).

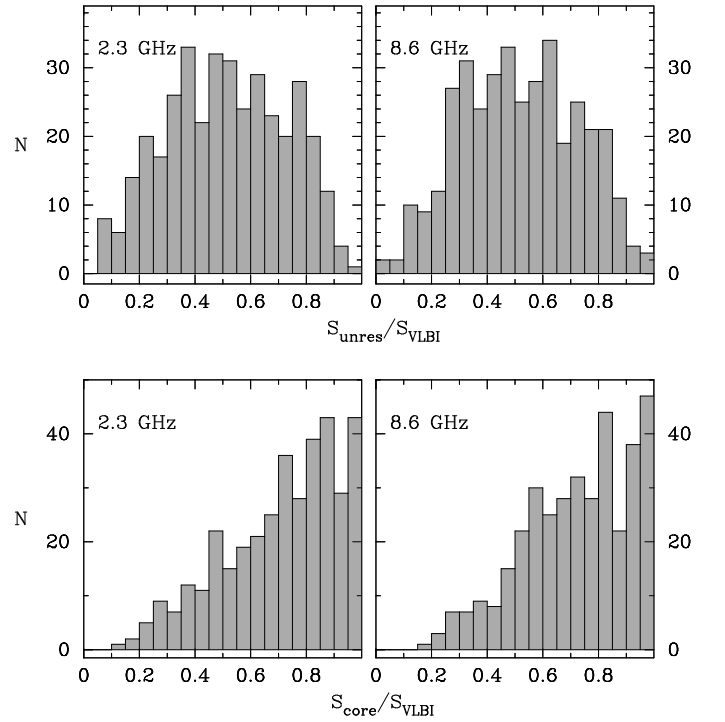


Figure 10. Distributions of the compactness $S_{\text{unres}}/S_{\text{VLBI}}$ (*top panels*) and the VLBI core dominance $S_{\text{core}}/S_{\text{VLBI}}$ (*bottom panels*).

is smaller than the respective resolution limit (a function of the restoring beam parameters and signal-to-noise ratio at the core position) calculated following Kovalev et al. (2005). The resolution limits have been used as upper limits of the component sizes. Overall, near one-fourth of the cores were unresolved,

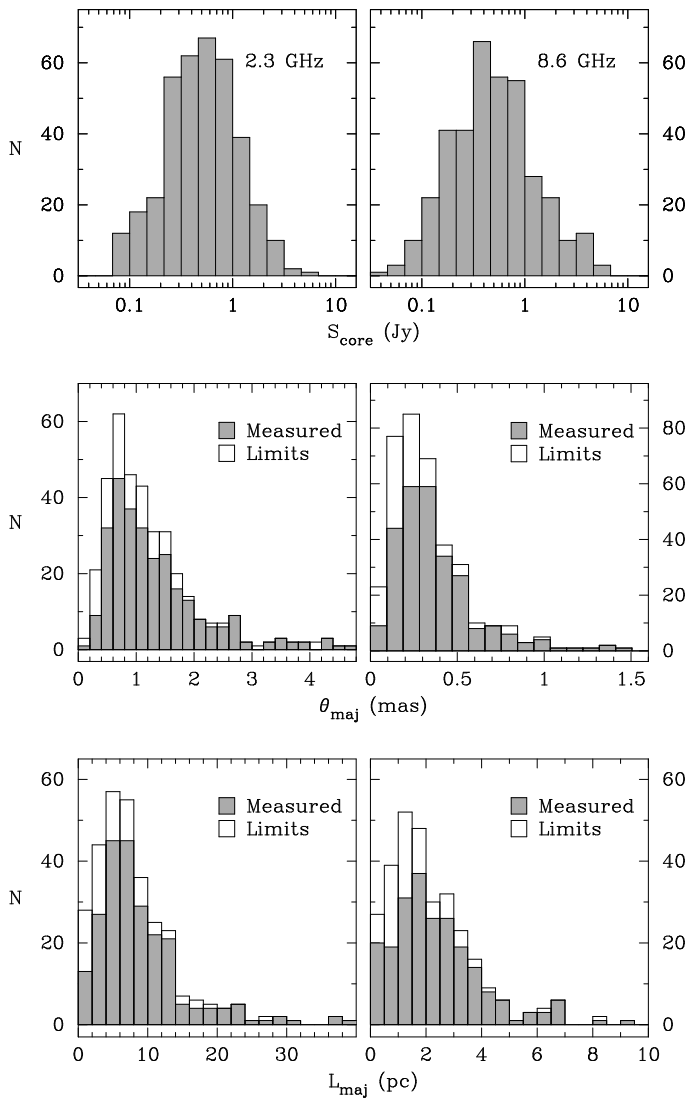


Figure 11. Distributions of flux (*top*), angular size (*middle*), and projected linear size (*bottom*) for the core components at 2.3 GHz (*left*) and 8.6 GHz (*right*). The unshaded boxes represent upper limits for those sources with unresolved core component. For the core components fitted with elliptical Gaussians, the major axis is used for the angular core size.

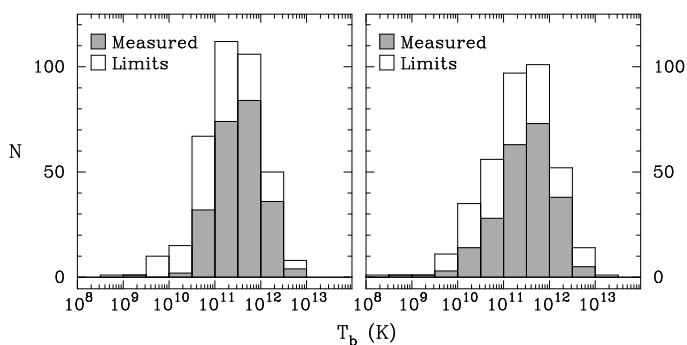


Figure 12. Brightness temperature distribution of VLBI core components in source rest frame at 2.3 GHz (*left*) and 8.6 GHz (*right*) with median value of 2.51×10^{11} K and 2.60×10^{11} K, respectively. The unshaded boxes represent lower limits for those sources with either unknown redshift or unresolved core component.

namely 98 at X-band and 87 at S-band. The projected linear sizes can also be calculated for the sources with known redshifts. The corresponding distributions of the angular and projected linear sizes of the VLBI core components are presented in Fig. 11 (middle and bottom panels), with median values of 0.28 mas (1.90 pc) and 1.04 mas (6.75 pc) at X-band and S-band measurements, respectively.

The brightness temperature of the core components in the source rest frame is given by (e.g., Kovalev et al. 2005)

$$T_{b, \text{core}} = \frac{2 \ln 2}{\pi k} \frac{S_{\text{core}} \lambda^2 (1+z)}{\theta_{\text{maj}} \theta_{\text{min}}}, \quad (1)$$

where k is the Boltzmann constant, S_{core} is the VLBI core flux density, θ_{maj} and θ_{min} are the FWHM of the elliptical Gaussian component along the major and the minor axes, λ is the wavelength of observation, z is the redshift. Measuring flux density in Jy, component sizes in mas, and wavelength in cm, we obtain

$$T_{b, \text{core}} = a_{\lambda} \frac{S_{\text{core}} (1+z)}{\theta_{\text{maj}} \theta_{\text{min}}} \text{ K}, \quad (2)$$

where $a_{\lambda} = 1.639 \times 10^{10}$ for X-band ($\lambda = 3.5$ cm) and $a_{\lambda} = 2.337 \times 10^{11}$ for S-band ($\lambda = 13$ cm). For sources without measured redshifts (see Table 1) we used $z = 0$ to determine a lower limit of the brightness temperature. Another fraction of sources that also yielded lower limits on the T_b values was a category of objects with unresolved cores. Altogether, about 40% of T_b values are the lower limits.

The distributions of brightness temperature of the VLBI cores at 2.3 and 8.6 GHz shown in Fig. 12 are broad covering more than four orders of magnitude with the median value of 2.5×10^{11} K at both frequencies, which is close to the equipartition value of $\sim 5 \times 10^{11}$ K (Readhead 1994) and to the inverse Compton limit of $\sim 10^{12}$ K (Kellermann & Pauliny-Toth 1969). The higher brightness temperatures may be explained by Doppler boosting (e.g., Kovalev et al. 2005; Homan et al. 2006; Cohen et al. 2007; Kellermann et al. 2007). The histograms in Fig. 12 obtained at different frequencies, 2 and 8 GHz, look similar because the maximum measurable T_b is determined by the physical length of the effective projected baseline and the core flux density (e.g., Kovalev et al. 2005; Kovalev 2009b). Therefore, for VLBI observations simultaneously made at different frequencies we would expect to obtain close T_b values, taking into account the flat radio spectra of the core components in most cases. The VLBI core parameters, such as fitted flux density, sizes or estimated resolution limits, and derived brightness temperature separately for 2.3 and 8.6 GHz are listed in Table 7. The statistics of the distributions shown in Figs. 9–12 are summarized in Table 8. Mean values for the distributions θ_{maj} , L_{maj} , and T_b were calculated using the ASURV survival analysis package (Lavalley et al. 1992).

3.5. Spectral properties

Flux density and parsec-scale structure variations in AGN jets require the observations to be carried out simultaneously at different frequencies in order to properly investigate the spectral properties of the sources. The RDV observations perfectly fulfill this requirement and enable us to study spectral characteristics of the observed sources by using (i) detailed approach through constructing and analyzing a spectral index distribution map of a source and (ii) also applying statistical methods to derive general spectral properties and possible correlations/trends. In this

Table 7. VLBI core component properties.

Source	Epoch	2.3 GHz				8.6 GHz			
		S_{core} Jy	θ_{maj} mas	θ_{min} mas	T_{b} K	S_{core} Jy	θ_{maj} mas	θ_{min} mas	T_{b} K
(1)	(2)	(3)	(4)	(5)	(6)	(7)	(8)	(9)	(10)
J0006–0623	2002/03/06	1.53	1.87	1.74	1.48e+11	1.55	0.81	0.27	1.56e+11
J0011–2612	1999/03/08	0.40	0.57	0.57	6.10e+11	0.33	0.35	<0.35	>8.92e+10
J0017+8135	2002/03/06	0.56	1.00	0.60	9.60e+11	0.54	0.41	0.18	5.16e+11
J0019+7327	1999/03/08	0.68	1.51	0.84	3.51e+11	0.14	0.52	0.52	2.36e+10
J0022+0608	2002/01/16	0.44	1.19	0.62	>1.39e+11	0.41	0.16	0.16	>2.55e+11
J0027+5958	2001/10/29	0.08	0.82	<0.82	>2.62e+10	0.08	0.20	<0.20	>2.97e+10
J0035+6130	2002/12/11	0.09	1.93	<1.55	>6.97e+09	0.09	0.45	0.45	>7.29e+09
J0050–0929	2002/03/06	0.56	1.66	0.92	>8.61e+10	0.74	0.55	0.19	>1.19e+11
J0059+0006	1999/05/10	0.29	1.41	1.41	5.83e+10	0.10	0.55	<0.55	>9.39e+09
J0102+5824	2002/01/16	0.57	0.96	0.72	3.17e+11	1.54	0.09	<0.07	>6.89e+12

Columns are as follows: (1) source name (J2000.0), (2) date of observations (YYYY/MM/DD), (3) fitted Gaussian core flux density, (4) FWHM major axis of the fitted core Gaussian, (5) FWHM minor axis of the fitted core Gaussian, (6) core brightness temperature, (7)–(10) the same as (3)–(6), respectively. Table 7 is published in its entirety in the electronic version of the *Astronomy & Astrophysics*. A portion is shown here for guidance regarding its form and content.

Table 8. Statistics of distributions in Figs. 9–12.

Frequency, [GHz]	S_{VLBI} , [Jy]		S_{unres} , [Jy]		$S_{\text{unres}}/S_{\text{VLBI}}$		$S_{\text{core}}/S_{\text{VLBI}}$	
	Mean	Median	Mean	Median	Mean	Median	Mean	Median
2.3	1.02 ± 0.08	0.76	0.47 ± 0.03	0.34	0.51 ± 0.02	0.51	0.72 ± 0.02	0.75
8.6	1.04 ± 0.10	0.69	0.54 ± 0.05	0.32	0.52 ± 0.02	0.51	0.73 ± 0.02	0.75
	S_{core} , [Jy]		θ_{core} , [mas]		$L_{\text{core proj}}$, [pc]		$\log(T_{\text{b, core}})$, [K]	
	Mean	Median	Mean	Median	Mean	Median	Mean	Median
2.3	0.69 ± 0.05	0.49	1.18 ± 0.09	1.04	7.56 ± 0.66	6.75	11.68 ± 0.05	11.40
8.6	0.76 ± 0.08	0.47	0.33 ± 0.03	0.28	2.18 ± 0.24	1.90	11.69 ± 0.07	11.41

paper, we mostly implement the latter approach. For the statistical analysis, we have used the calculated values of total VLBI flux densities from the 2.3 and 8.6 GHz images (see Table 5) to derive the integrated spectral index. The vast majority of sources have flat spectra, $\alpha > -0.5$ for more than 95% of the sample (Fig. 13, top).

We have also derived median spectral indices for the VLBI jets applying the following procedure. First, for each source the X- and S-band images were obtained with the same pixel size (0.2 mas) and the same resolution convolving them with the average restoring beam. Spectral index map was obtained by aligning optically thin parts of the jet. Then, using the X-band data, the total intensity jet ridge line was constructed with nearly equally spaced points separated by a distance of the pixel size. The procedure stops where the peak of a Gaussian curve fitted to the transverse jet profile becomes less than 4rms noise level of the image. The position of the core component taken from the model fit was chosen as a starting point. Note that the VLBI core is often but not always is the brightest feature on the map. Thus, the image phase center, where the CLEAN algorithm tends to place the brightest component, would be a wrong choice of the starting point in such cases. Applying the ridge line to the spectral index distribution map, we extracted the values of α along the jet. After that we masked out the core region within $r_{\text{core}} < 0.5(b_{\phi}^2 + d_{\phi}^2)^{0.5}$, where b_{ϕ} and d_{ϕ} are the beam and fitted core sizes, respectively, along a position angle ϕ of the inner jet. Finally, the jet spectral index was estimated as the median of the rest values. The described method provided the results for 319 sources. Other 51 objects do not have enough

structure, making the application of the procedure impossible. The obtained assessments of the jet spectral indices are mostly distributed in a range from -0.2 to -1.2 with the median value of $\alpha_{2-8}^{\text{jet}} = -0.68$, indicating optically thin radiation (Fig. 13, bottom). Spectral index of optically thin synchrotron radiation parametrizes the energy spectrum of relativistic radiative particles. Assuming a power-law energy distribution $N(E) = N_0 E^{-\gamma}$, the power index $\gamma = 1 - 2\alpha$ has the median value of $\gamma = 2.4$ in the jets from the studied sample. The only positive value of a median jet spectral index was registered for the quasar J0927+3902, which has a short (~ 3 mas) jet with a resolved feature several times brighter than the core at both frequencies. This feature that dominates in the structure is optically thick at 2 and 8 GHz and has a spectral index of 0.36. See also Kovalev et al. (1999) for the simultaneous total flux spectrum of the object.

Spectral index on average decreases along the jet ridge line (Fig. 14) due to the spectral aging caused by radiative losses of electrons. It slightly flattens in bright jet knots which might be explained by shock acceleration at least in some cases. Using linear least square method, we estimated the spectral index gradients in the jets of 228 sources (Fig. 15). This analysis was done only for sources with at least 10 ridge line points beyond the core region. The mean value of the spectral index gradient is $-0.06^{+0.07}_{-0.08}$ mas $^{-1}$, where the errors are given at the 68% confidence level.

Spectral indices for the VLBI cores were obtained as a value of α -map at pixel corresponding to the starting point of the ridge line (X-band core). The distribution of the core spectral indices

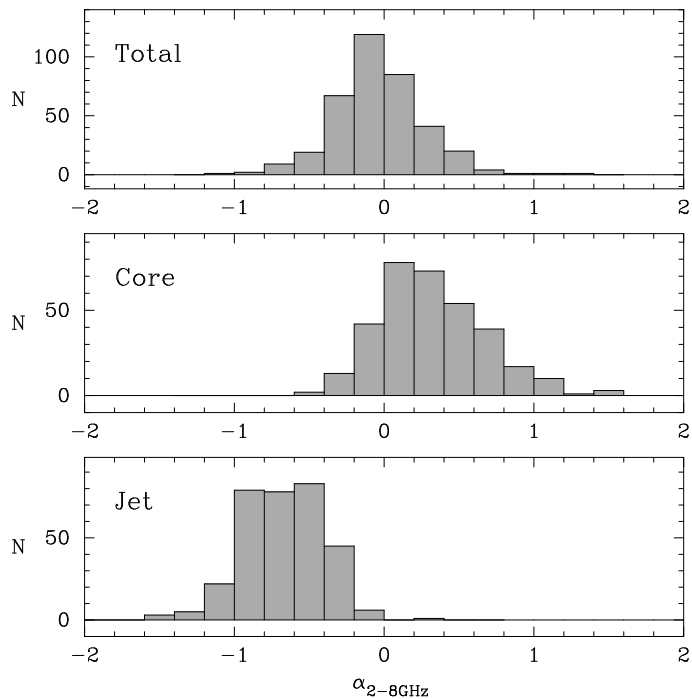


Figure 13. Distributions of the 2.3–8.6 GHz spectral index of total VLBI scale emission (*top*), VLBI cores (*middle*), and jets (*bottom*).

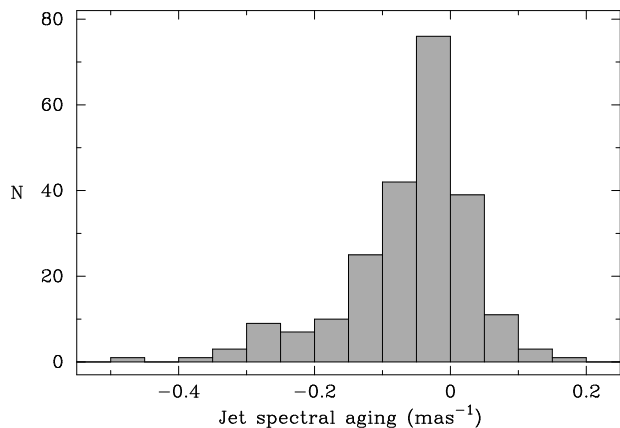


Figure 15. Distribution of spectral index gradient along total intensity ridge line for 228 sources.

(Fig. 13, middle) has the median value of $\alpha_{2-8}^{\text{core}} = 0.28$ reflecting that the cores are partially opaque.

We also examined the connection between total spectral index and milliarcsecond compactness. The results for X-band data are shown in Fig. 16, the S-band dependence is qualitatively similar. The non-parametric Kendall's τ -test confirms a positive correlation at a confidence level 99.9%. The explanation for this visible trend is that sources with steeper spectra are expected to have lower compactness indices, because a significant fraction of their VLBI flux should originate from optically thin extended jet emission.

3.6. Brightness temperature evolution along jets

The sources with the prominent jets were the cases of our particular interest, since they allow to investigate the evolution of brightness temperature along the jet both as a function of dis-

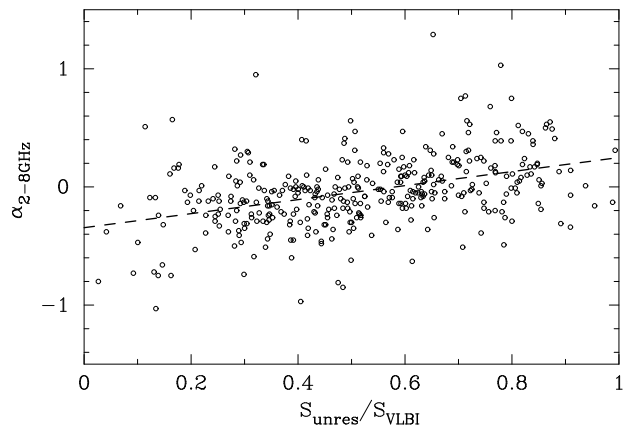


Figure 16. Integral spectral index versus milliarcsecond compactness index at 8.6 GHz. The trend reflects the tendency for steep spectrum sources to be less compact.

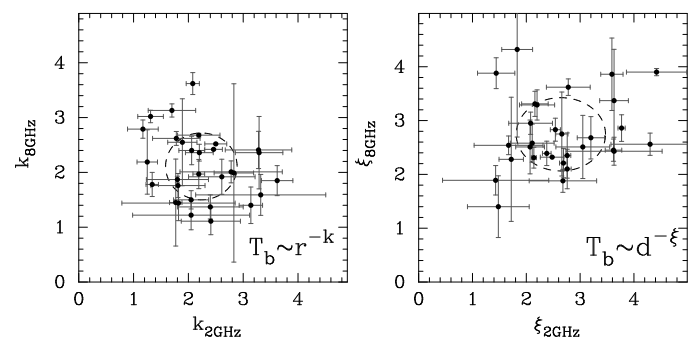


Figure 17. 8.6 vs 2.3 GHz power-law indices of brightness temperature gradients with distance to the core (*left*) and with jet component size (*right*). The dashed ellipse represents 1σ error area of k - and ξ -index distributions.

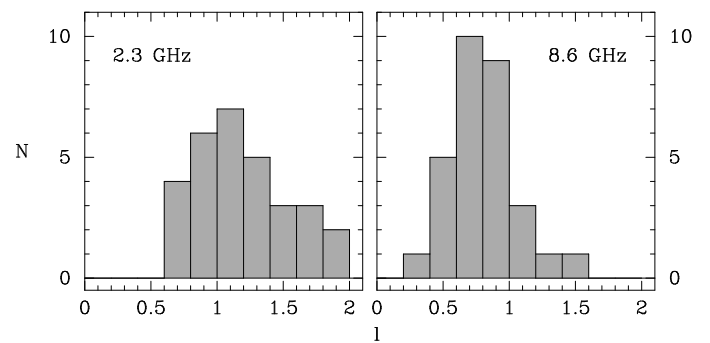


Figure 18. Distributions of a power index l assuming a $d \propto r^l$ dependence, where d is the transverse width of the jet at a distance r from its apparent origin at 2.3 GHz (*left*) and 8.6 GHz (*right*).

tance to the core r , and the component's size d . Typically, a blob of relativistic plasma, registered on a VLBI map as a bright jet component, intensively loses energy through synchrotron radiation and adiabatic expansion and quickly becomes dim propagating down the outflow and increasing in size. These factors lead to the rapid decrease of brightness temperature along the jet. Evolution of T_b can be well fitted by a simple power-law functions $T_b \propto r^{-k}$ and $T_b \propto d^{-\xi}$. We have analyzed the brightness temperature gradients for 30 sources with a rich jet structure consisting of at least three model fitted jet components at both

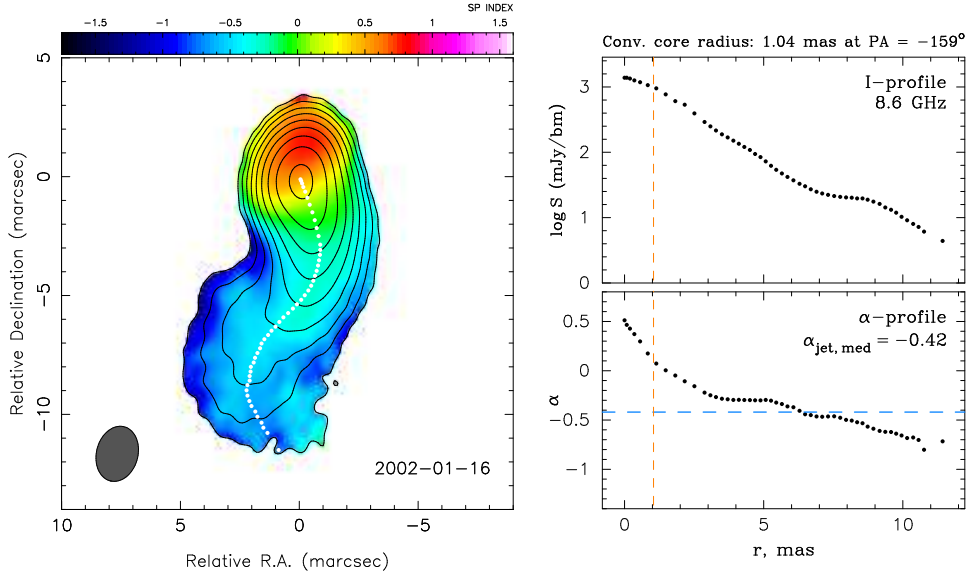


Figure 14. Spectral index distribution in J2202+4216 (left) calculated between 2.3 and 8.6 GHz with the 8.6 GHz total intensity contours overlaid. White dots represent the total intensity ridge line, along which we plot the profiles of total intensity (top right) and spectral index (bottom right). The lowest contour is plotted at 0.18% of the peak brightness of $1395 \text{ mJy beam}^{-1}$. The shaded ellipse represents the FWHM of the restoring beam of $2.34 \times 1.74 \text{ mas}$ at $\text{PA} = -14.0^\circ$, derived as the average between the corresponding interferometric restoring beams at 8.6 and 2.3 GHz. The vertical orange dashed line shows the convolved radius of the VLBI core calculated along the inner jet direction.

frequencies. The power-law index k varies between 1.2 and 3.6, with the average value of $k_{8 \text{ GHz}} \approx k_{2 \text{ GHz}} = 2.2 \pm 0.1$. The power-law index ξ varies between 1.4 and 4.4, with the average value of $\xi_{8 \text{ GHz}} = 2.7 \pm 0.1$ and $\xi_{2 \text{ GHz}} = 2.6 \pm 0.1$. Distributions of the fitted power indices k and ξ are shown in Fig. 17. The power indices k and ξ can be further used to test jet models, e.g. adiabatic expansion in a shock-in-jet model suggested by Marscher (1990).

Assuming a power law dependence of the width of a jet with distance as $d \propto r^l$, the power law index l can be readily estimated as k/ξ . The obtained distributions of l (Fig. 18) have median values of 1.2 at S-band and 0.8 at X-band, suggesting that jet regions probed by the RDV observations at 8.6 GHz are still collimating and therefore accelerating, while at 2.3 GHz the jets are more freely expanding and switch to a deceleration regime. It is consistent with positive parallel accelerations detected by Piner et al. (2012) analyzing 10 year jet kinematics based on the 8.6 GHz RDV data and also by Homan et al. (2009) for 15 GHz MOJAVE data.

3.7. Gamma-ray bright AGN at parsec scales

Out of the 370 objects analyzed in this paper, 147 sources (40%, see Table 1) have been positionally associated with γ -ray detections within their corresponding 95% confidence region made by the Large Area Telescope (LAT) on board the *Fermi* Observatory at energies above 100 MeV within two years of scientific operations (Abdo et al. 2011). The list of the 147 sources include 99 out of 251 quasars (40%), 39 out of 46 BL Lacs (85%), 6 out of 31 radio galaxies (20%), and 3 out of 42 optically unidentified sources (7%). A significantly higher detection rate for BL Lacs is explained by their harder spectra, which allows them to be detected by the *Fermi* LAT more easily (Ackermann et al. 2011). It also should be noted that the vast majority of γ -ray detections associated with AGN have significant radio flux densities at parsec scales as indicated by highly successful identifications of the

Fermi LAT objects with radio parsec-scale catalog of extragalactic jets (Kovalev 2009a). The *Fermi* era has already heralded a number of important links between γ -ray emission and parsec-scale properties of AGN. It has been shown that LAT-detected sources are brighter and more luminous (Kovalev et al. 2009), have higher apparent jet speeds (Lister et al. 2009b; Piner et al. 2012), higher Doppler factors (Savolainen et al. 2010), and characterized by wider apparent opening angles (Pushkarev et al. 2009). There is also a number of evidences for γ -ray emission to likely originate in the base of relativistic jet close to parsec-scale radio core (e.g., Kovalev et al. 2009; Jorstad & Marscher 2010; Pushkarev et al. 2010).

We have compared flux densities of the VLBI core components for the LAT detected versus non-LAT detected RDV sources (Fig. 19) and found that the γ -ray bright sources have higher radio core fluxes, with a mean value of 0.89 Jy versus 0.56 Jy at 2.3 GHz and 1.08 Jy versus 0.55 Jy at 8.6 GHz. In both cases, Kolmogorov-Smirnov test indicates a probability $p < 0.001$ for the corresponding samples being drawn from the same parent population. For the further investigation of γ -ray/radio jet relation, we have also examined the core brightness temperature $T_{\text{b, core}}$. Gehan's generalized Wilcoxon test from the ASURV survival analysis package indicates, at a $> 99.9\%$ confidence, that the $T_{\text{b, core}}$ values for LAT-detected sources are statistically higher than those for the rest of the sample at 8.6 GHz (Fig. 20, right) suggesting higher Doppler-boosting factors. For the 2.3 GHz data, the difference is marginal (92.3% confidence) possibly due to different spectral properties of the radio core and innermost jet components not resolved with lower frequency observations. These findings confirm the early results reported by Kovalev et al. (2009).

Additionally, we examined the distribution of the median spectral indices for the VLBI jets obtained as described in § 3.5. The distributions of α_{jet} for 135 LAT-detected and 184 non-LAT-detected sources (Fig. 21) are different at the significance level of 99.8% as indicated by K-S test. The corresponding medians

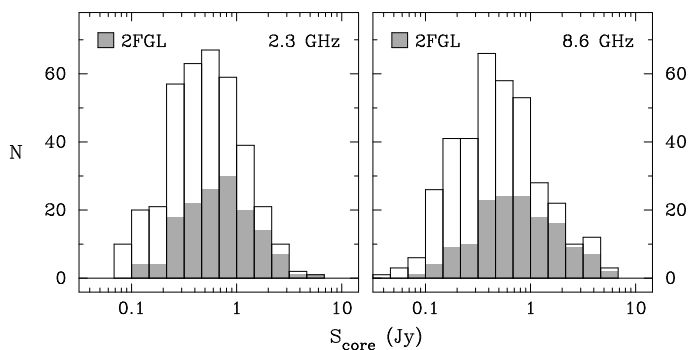


Figure 19. Flux density distributions of VLBI core components at 2.3 GHz (*left*) and 8.6 GHz (*right*). The shaded areas represent LAT-detected (2FGL) sources.

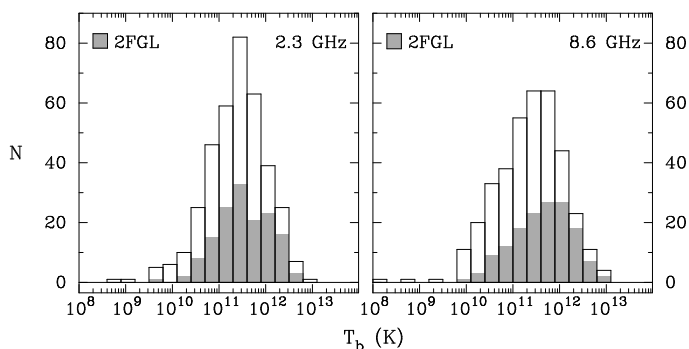


Figure 20. Brightness temperature distributions of VLBI core components at 2.3 GHz (*left*) and 8.6 GHz (*right*). The shaded areas represent LAT-detected (2FGL) sources.

are $\alpha_{\text{LAT-Y}} = -0.60$ and $\alpha_{\text{LAT-N}} = -0.72$ that correspond to the power index $\gamma_{\text{LAT-Y}} = 2.20$ and $\gamma_{\text{LAT-N}} = 2.44$ of the energy spectrum of relativistic radiative particles. This difference is explained by a larger fraction of high-energy synchrotron emitting electrons in γ -ray bright AGN produced by either more energetic or more frequent flares.

4. Conclusions

We have obtained single-epoch images for a sample of 370 AGN based on the global VLBI observations carried out simultaneously at 2.3 and 8.6 GHz with a participation of ten VLBA antennas and up to ten additional geodetic radio telescopes. Parameters of Gaussian model components representing the source structure are also determined. The sample contains 251 quasars, 46 BL Lacertae objects, 31 radio galaxies, and 42 optically unidentified sources. At least 97% of the sources show one-sided core-jet structure suggesting small angle to the line of sight. Even at milliarcsecond scales the sources are highly compact and strongly core-dominated. Almost one-fourth of the core components are completely unresolved on the longest baselines of the global VLBI observations.

Of the 370 observed sources, 96% have flat-spectrum partially opaque cores with a median value of spectral index of $\alpha_{\text{core}} \sim 0.3$. The jet components are usually optically thin with a median value of $\alpha_{\text{jet}} \sim -0.7$ that corresponds to $\gamma \sim 2.4$ assuming a power-law energy distribution $N(E) = N_0 E^{-\gamma}$ of radiative particles. Spectral index on average decreases along the jet ridge line due to the spectral aging. It slightly flattens in bright jet knots which might be explained by shock acceleration at least in some cases. Estimated brightness temperatures of the VLBI

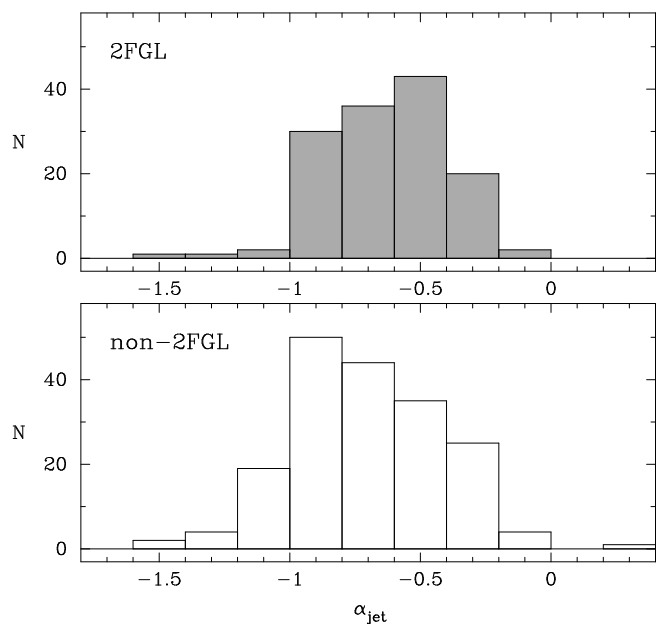


Figure 21. Distribution of the 2.3–8.6 GHz spectral index for the VLBI jets detected (*top*) and not detected (*bottom*) by the *Fermi* LAT. See discussion of the positive value found for the quasar J0927+3902 in Sec. 3.5.

cores are affected by Doppler boosting, their typical values are found at the level of 10^{11} K, reaching up to 10^{13} K in rare cases. We note that 40% of measurements yield only lower limits either because of unknown redshift or unresolved core component. No systematic difference was registered for values of $T_{\text{b, core}}$ obtained at 2.3 and 8.6 GHz.

The evolution of the brightness temperature of the jet components as a function of distance to the core, r , and transverse size, d , was fitted with power-law dependencies $T_{\text{b}} \propto r^{-k}$ and $T_{\text{b}} \propto d^{-\xi}$, respectively, for 30 sources with straight and prominent jets, for which the mean values of $k_{8\text{GHz}} \approx k_{2\text{GHz}} = 2.2$ and $\xi_{8\text{GHz}} = 2.7$, $\xi_{2\text{GHz}} = 2.6$ that can be further used to test jet models. At the scales probed by 8.6 GHz observations, a jet geometry for these sources shows an evidence for further jet collimation, while at the larger scales probed by 2.3 GHz observations, the outflows are expanding more freely, perhaps switching the deceleration regime.

Out of the 370 presented sources, 147 (40%) positionally associated with high-confidence γ -ray detections from the *Fermi* LAT Second Source Catalog are found to have higher core flux densities and brightness temperatures suggesting preferentially higher Doppler-boosting factors. Furthermore, we have found that the LAT-detected AGN are characterized by less steep radio spectrum of the optically thin jet emission, most probably due to a larger fraction of high-energy radio emitting electrons produced by flares.

The obtained VLBI images together with respective Gaussian models may be used for astrometric tasks on improving source positions by taking into account their milliarcsecond structure. The highly-compact bright sources would be potentially the best targets for space VLBI studies with the *RadioAstron* mission (Kardashev 1997).

Acknowledgements. We would like to thank R. Porcas, A. Lobanov, L. Petrov, T. Savolainen, and G. Piner for useful discussions. This work is based on the analysis of global VLBI observations including the VLBA, the raw data for which were provided to us by the NRAO archive. The National Radio Astronomy Observatory is a facility of the National Science Foundation operated under

cooperative agreement by Associated Universities, Inc. YYK is partly supported by the Russian Foundation for Basic Research (project 11-02-00368) and Dynasty Foundation. This research has made use of NASA's Astrophysics Data System. This research has made use of the NASA/IPAC Extragalactic Database (NED) which is operated by the Jet Propulsion Laboratory, California Institute of Technology, under contract with National Aeronautics and Space Administration.

References

- Abdo, A. A., Ackermann, M., Ajello, M., & et al. 2011, arXiv:1108.1435
- Ackermann, M., Ajello, M., Allafort, A., et al. 2011, *ApJ*, 743, 171
- Afanasiev, V. L., Dodonov, S. N., Moiseev, A. V., et al. 2003, *Astronomy Reports*, 47, 458
- Beasley, A. J., Gordon, D., Peck, A. B., et al. 2002, *ApJS*, 141, 13
- Best, P. N., Peacock, J. A., Brookes, M. H., et al. 2003, *MNRAS*, 346, 1021
- Boboltz, D. A., Gaume, R. A., Fey, A. L., et al. 2010, in *Bulletin of the American Astronomical Society*, Vol. 42, American Astronomical Society Meeting Abstracts #215, 512
- Carilli, C. L., Menten, K. M., Reid, M. J., Rupen, M. P., & Yun, M. S. 1998, *ApJ*, 494, 175
- Charlot, P., Boboltz, D. A., Fey, A. L., et al. 2010, *AJ*, 139, 1713
- Charlot, P., Fey, A. L., Collioud, A., et al. 2008, in *IAU Symposium*, Vol. 248, IAU Symposium, ed. W. J. Jin, I. Platais, & M. A. C. Perryman, 344–347
- Cohen, M. H., Lister, M. L., Homan, D. C., et al. 2007, *ApJ*, 658, 232
- Cornwell, T. J. & Wilkinson, P. N. 1981, *MNRAS*, 196, 1067
- Dodson, R., Fomalont, E. B., Wiik, K., et al. 2008, *ApJS*, 175, 314
- Drake, C. L., Bicknell, G. V., McGregor, P. J., & Dopita, M. A. 2004, *AJ*, 128, 969
- Fey, A. L. & Charlot, P. 1997, *ApJS*, 111, 95
- Fey, A. L. & Charlot, P. 2000, *ApJS*, 128, 17
- Fey, A. L., Clegg, A. W., & Fomalont, E. B. 1996, *ApJS*, 105, 299
- Fey, A. L., Ma, C., Arias, E. F., et al. 2004, *AJ*, 127, 3587
- Fomalont, E. B., Frey, S., Paragi, Z., et al. 2000, *ApJS*, 131, 95
- Fomalont, E. B., Petrov, L., MacMillan, D. S., Gordon, D., & Ma, C. 2003, *AJ*, 126, 2562
- Gabuzda, D. C., Pushkarev, A. B., & Cawthorne, T. V. 2000, *MNRAS*, 319, 1109
- Greisen, E. W. 2003, in *Astrophysics and Space Science Library* 285, *Information Handling in Astronomy – Historical Vistas*, ed. A. Heck (Dordrecht: Kluwer), 109
- Helmboldt, J. F., Taylor, G. B., Tremblay, S., et al. 2007, *ApJ*, 658, 203
- Hewitt, A. & Burbidge, G. 1989, in *A new optical catalog of QSO (1989)*
- Högbom, J. A. 1974, *A&AS*, 15, 417
- Homan, D. C., Kadler, M., Kellermann, K. I., et al. 2009, *ApJ*, 706, 1253
- Homan, D. C., Kovalev, Y. Y., Lister, M. L., et al. 2006, *ApJ*, 642, L115
- Jennison, R. C. 1958, *MNRAS*, 118, 276
- Jorstad, S. G. & Marscher, A. P. 2010, in *Bulletin of the American Astronomical Society*, Vol. 42, American Astronomical Society Meeting Abstracts 215, 225.02
- Kardashev, N. S. 1997, *Experimental Astronomy*, 7, 329
- Kellermann, K. I., Kovalev, Y. Y., Lister, M. L., et al. 2007, *Ap&SS*, 311, 231
- Kellermann, K. I. & Pauliny-Toth, I. I. K. 1969, *ApJ*, 155, L71
- Kellermann, K. I., Vermeulen, R. C., Zensus, J. A., & Cohen, M. H. 1998, *AJ*, 115, 1295
- Kovalev, Y. Y. 2009a, *ApJ*, 707, L56
- Kovalev, Y. Y. 2009b, in *Astronomical Society of the Pacific Conference Series*, Vol. 402, *Approaching Micro-Arcsecond Resolution with VSOP-2: Astrophysics and Technologies*, ed. Y. Hagiwara, E. Fomalont, M. Tsuboi, & M. Yasuhiro, 179
- Kovalev, Y. Y., Aller, H. D., Aller, M. F., et al. 2009, *ApJ*, 696, L17
- Kovalev, Y. Y., Kellermann, K. I., Lister, M. L., et al. 2005, *AJ*, 130, 2473
- Kovalev, Y. Y., Lobanov, A. P., Pushkarev, A. B., & Zensus, J. A. 2008, *A&A*, 483, 759
- Kovalev, Y. Y., Nizhelsky, N. A., Kovalev, Y. A., et al. 1999, *A&AS*, 139, 545
- Kovalev, Y. Y., Petrov, L., Fomalont, E. B., & Gordon, D. 2007, *AJ*, 133, 1236
- Lanyi, G. E., Boboltz, D. A., Charlot, P., et al. 2010, *AJ*, 139, 1695
- Lavalley, M., Isobe, T., & Feigelson, E. 1992, in *Astronomical Society of the Pacific Conference Series*, Vol. 25, *Astronomical Data Analysis Software and Systems I*, ed. D. M. Worrall, C. Biemesderfer, & J. Barnes, 245–247
- Lee, S.-S., Lobanov, A. P., Krichbaum, T. P., et al. 2008, *AJ*, 136, 159
- Lister, M. L., Aller, H. D., Aller, M. F., et al. 2009a, *AJ*, 137, 3718
- Lister, M. L., Homan, D. C., Kadler, M., et al. 2009b, *ApJ*, 696, L22
- Lister, M. L. & Marscher, A. P. 1997, *ApJ*, 476, 572
- Lobanov, A. P. 1998, *A&A*, 330, 79
- Ma, C., Arias, E. F., Eubanks, T. M., et al. 1998, *AJ*, 116, 516
- Marscher, A. P. 1990, in *Parsec-scale radio jets*, ed. J. A. Zensus & T. J. Pearson, 236
- Marscher, A. P. 2008, in *Astronomical Society of the Pacific Conference Series*, Vol. 386, *Extragalactic Jets: Theory and Observation from Radio to Gamma Ray*, ed. T. A. Rector & D. S. De Young, 437
- Nilsson, K., Pursimo, T., Sillanpää, A., Takalo, L. O., & Lindfors, E. 2008, *A&A*, 487, L29
- Pearson, T. J., Shepherd, M. C., Taylor, G. B., & Myers, S. T. 1994, *Bulletin of the American Astronomical Society*, 26, 1318
- Petrov, L., Gordon, D., Gipson, J., et al. 2009, *Journal of Geodesy*, 83, 859
- Petrov, L., Hirota, T., Honma, M., et al. 2007, *AJ*, 133, 2487
- Petrov, L., Honma, M., & Shibata, S. M. 2012, *AJ*, 143, 35
- Petrov, L., Kovalev, Y. Y., Fomalont, E. B., & Gordon, D. 2005, *AJ*, 129, 1163
- Petrov, L., Kovalev, Y. Y., Fomalont, E. B., & Gordon, D. 2006, *AJ*, 131, 1872
- Petrov, L., Kovalev, Y. Y., Fomalont, E. B., & Gordon, D. 2008, *AJ*, 136, 580
- Petrov, L. & Taylor, G. B. 2011, *AJ*, 142, 89
- Piner, B. G., Mahmud, M., Fey, A. L., & Gospodinova, K. 2007, *AJ*, 133, 2357
- Piner, B. G., Pushkarev, A. B., Kovalev, Y. Y., et al. 2012, *ApJ*, in prep.
- Pollack, L. K., Taylor, G. B., & Zavala, R. T. 2003, *ApJ*, 589, 733
- Popov, M. V. & Kovalev, Y. Y. 1999, *Astronomy Reports*, 43, 561
- Pushkarev, A. B., Kovalev, Y. Y., & Lister, M. L. 2010, *ApJ*, 722, L7
- Pushkarev, A. B., Kovalev, Y. Y., Lister, M. L., & Savolainen, T. 2009, *A&A*, 507, L33
- Readhead, A. C. S. 1994, *ApJ*, 426, 51
- Readhead, A. C. S., Walker, R. C., Pearson, T. J., & Cohen, M. H. 1980, *Nature*, 285, 137
- Savolainen, T., Homan, D. C., Hovatta, T., et al. 2010, *A&A*, 512, A24
- Schwab, F. R. 1980, in *Society of Photo-Optical Instrumentation Engineers (SPIE) Conference Series*, Vol. 231, *Society of Photo-Optical Instrumentation Engineers (SPIE) Conference Series*, ed. W. T. Rhodes, 18–25
- Shepherd, M. C. 1997, in *Astronomical Society of the Pacific Conference Series*, Vol. 125, *Astronomical Data Analysis Software and Systems VI*, ed. G. Hunt & H. E. Payne (San Francisco: ASP), 77
- Snellen, I. A. G., Lehnert, M. D., Bremer, M. N., & Schilizzi, R. T. 2002a, *MNRAS*, 337, 981
- Snellen, I. A. G., McMahon, R. G., Hook, I. M., & Browne, I. W. A. 2002b, *MNRAS*, 329, 700
- Sokolovsky, K. V., Kovalev, Y. Y., Pushkarev, A. B., & Lobanov, A. P. 2011, *A&A*, 532, A38
- Sowards-Emmerd, D., Romani, R. W., Michelson, P. F., Healey, S. E., & Nolan, P. L. 2005, *ApJ*, 626, 95
- Twiss, R. Q., Carter, A. W. L., & Little, A. G. 1960, *The Observatory*, 80, 153
- Véron-Cetty, M.-P. & Véron, P. 2006, *A&A*, 455, 773
- von Montigny, C., Bertsch, D. L., Chiang, J., et al. 1995, *ApJ*, 440, 525